



# Limits and artefacts of reflective imaging goniophotometers for complex solar façade systems

**Boris Karamata<sup>\*1</sup> and Marilyne Andersen<sup>1</sup>**

<sup>1</sup> Interdisciplinary Laboratory of Performance-Integrated Design,  
Ecole Polytechnique Fédérale de Lausanne (EPFL), Lausanne, Switzerland

<sup>\*</sup> Corresponding author, boris.karamata@epfl.ch

## Abstract

The design of systems for solar light collection, modulation and/or distribution requires a thorough knowledge of their optical properties. The angular distribution of the scattered incident light flux, described by the Bidirectional Scattering Distribution Function (BSDF), can be measured with a step-by-step scanning goniophotometer but requires considerable time, especially when aiming at high angular resolution over a wide range and numerous incidence angles like in typical solar applications. Considerably faster measurements can be achieved with a so-called imaging goniophotometer, which simultaneously measures light fluxes in all scattered directions by dispatching them over different portions of a two-dimensional sensor array.

In this contribution, we revisit the widely accepted principle of a reflective imaging goniophotometer (RIG), which is based on a hemispherical (or ellipsoidal) mirror and a fisheye camera. Specifically developed ray-tracing tools allowed us to obtain accurate figures relative to the influence of key design parameters on angular resolution. Our calculations reveal that the measurement accuracy is too low for samples larger than a few tens of millimeters. Most importantly, we found significant limitations and artefacts in the angular-to-spatial mapping function inherent to the RIG principle, which generally severely bias BSDF measurements.

## 1. Introduction

The energy conveyed by solar radiations can be exploited in various manners. Besides transformation into heat or electricity, a direct use for indoor lighting remains very appealing. Since artificial indoor lighting is commonly used during daytime, there is a strong incentive to reduce our consumption of energy with a better harvest and distribution of daylight. Moreover, a better control of the light flux and its spectral contents can reduce significantly the heating and cooling loads. Besides energy savings, natural light is healthier [1], more pleasant and bears the potential for aesthetical lighting.

Complex fenestration systems (CFS), made of increasingly sophisticated structures and materials, are developed to better control and exploit solar radiations while minimizing discomfort issues [2]. The benefits obtained with a complex solar façade can be assessed with computer simulations, mostly based on ray-tracing like Radiance [3]. Reliable simulations require an accurate knowledge of the optical properties of the CFS and of all other elements involved. Particular attention should be paid to the angular light distribution of the reflected or transmitted light flux, which can be described by the Bidirectional Scattering Distribution Function (BSDF), introduced by Nicodemus and further adopted by the CIE [4]. A thorough knowledge of the BSDF also allows the manufacturers to qualify and optimize their products.

There is an increasingly stronger need to rely on BSDF in many fields, for instance for modeling luminaires, CFSs, and objects in graphical computer simulations. In its simplest form, the BSDF is a

multidimensional function depending on four variables, which are the polar coordinates of the incidence and scattering angles,  $(\theta_i, \varphi_i)$  and  $(\theta_s, \varphi_s)$ , respectively. More dimensions may be included when accounting for the spectral distribution and(or) the polarization of light. In practice, for measurement and use, the BSDF is usually split into a Bidirectional Reflection Distribution Function (BRDF) and a Bidirectional Transmission Distribution Function (BTDF), describing the distribution of the reflected and transmitted light flux in the relevant hemispherical space, respectively. Thus, to measure a BT(R)DF( $\theta_i, \varphi_i, \theta_s, \varphi_s$ ), one needs to measure the scattering intensity distribution over  $2\pi$  steradians with the highest possible angular resolution, for each incident angles  $(\theta_i, \varphi_i)$  and possibly for different wavelength ranges. Such measurement is not straightforward and requires a dedicated instrument called a goniophotometer.

## 2. Scanning and imaging goniophotometers

Traditional goniophotometers generally consist of a two-axis mechanical scanner moving a photodetector around the sample in small angular steps across the hemispherical space [5]. Such scanning goniophotometer offer reliable and flexible measurements since the sampling accuracy, dynamical range and spectral response can be easily adjusted. The main drawback of the method is the long measurement time due to the large number of measurement points. For instance, a resolution of  $1^\circ$  across the whole hemispherical space requires around 20700 measurements. Assuming a time interval of one second between each measurement (displacement, stabilization and acquisition time), the measurement of a BT(R)DF would take nearly six hours for each single incidence angle. When aiming at characterizing many new CSFs under many incidence angles (typically 145 in daylighting modeling) and possibly for different spectral ranges, a drastic reduction of the measurement time is an absolute necessity.

Several orders of magnitude faster measurements can be achieved with a radically different type of goniophotometer, called imaging or video goniophotometer, which captures the entire scattered wavefront at once (no moving parts). Thanks to a specific optics, an imaging goniophotometer simultaneously measures light fluxes in all scattered directions by dispatching them over different portions of a two-dimensional sensor array [6]. Few ingenious designs of systems allowing such an angular-to-spatial mapping have so far been devised. Three types of working principles can be distinguished: (1) Fourier optics, (2) screen projection and imaging and (3) reflection and imaging. Instrument of the first category rely on a complex custom lens assembly performing the angular-to-spatial mapping by means of an optical Fourier transform [7]. The second category of instruments consists of a hemispherical (or cubical) screen intercepting light scattered over  $2\pi$  steradians. Light backscattered by the screen is then imaged on a sensor via a fisheye camera or via a convex mirror and lens system [8]. Excellent performance is obtained with commercial instruments belonging to these two categories. However, these instruments are restricted to relatively small samples. For specific applications, one needs to measure the average scattering properties over a large sample such as for instance a CFS, whose structures have characteristic sizes typically ranging between one to a few tens of centimeters.

In the third category, a relatively simple and ingenious imaging goniophotometer, proposed by Ward [9] and further developed by Andersen and al. [10], was specifically developed for measuring large samples at high speed. This so called reflective imaging goniophotometer (RIG), based on a hemispherical or ellipsoidal mirror and a fisheye camera, is endowed with very attractive features such as a high throughput and negligible stray light. However, although widely accepted, the RIG is still missing a full validation of its principle. In this contribution, we revisit the performance and limitations of the RIG, in particular when measuring relatively large samples.

### 3. Reflective imaging goniophotometer

#### 3.1. Working principle

The basic architecture of the RIG system is shown in figure 1. It consists of a semi-reflective ellipsoidal or hemispherical dome above the x-z plane with a sample and a fisheye camera positioned at  $F_1$  and  $F_2$ , respectively. The semi-reflective coating properties allow for an illumination from either below or above so as to get either BTDF or BRDF measurements.

The working principle rests on the geometrical properties of an ellipse, namely the stigmatic relationship between the two foci points  $F_1$  and  $F_2$ , and on the properties of a fisheye lens. With an ellipsoidal mirror, any optical ray leaving  $F_1$  is reflected by the dome inner surface so as to reach  $F_2$ . Thus, in the first approximation, all light scattered by a small sample positioned at  $F_1$  is redirected towards  $F_2$  after reflection on the ellipsoidal dome. The fisheye camera positioned at  $F_2$  (see Fig. 1) provides a direct angular-to-spatial mapping of the angular distribution of the reflected rays. Indeed, by design, each pixel of the sensor of the fisheye camera detects light from a specific direction. The angular distribution of the rays scattered by the sample at  $F_1$ , i.e. the BT(R)DF, can be calculated with geometrical rules from the angular distribution of the rays reflected towards  $F_2$  [9]

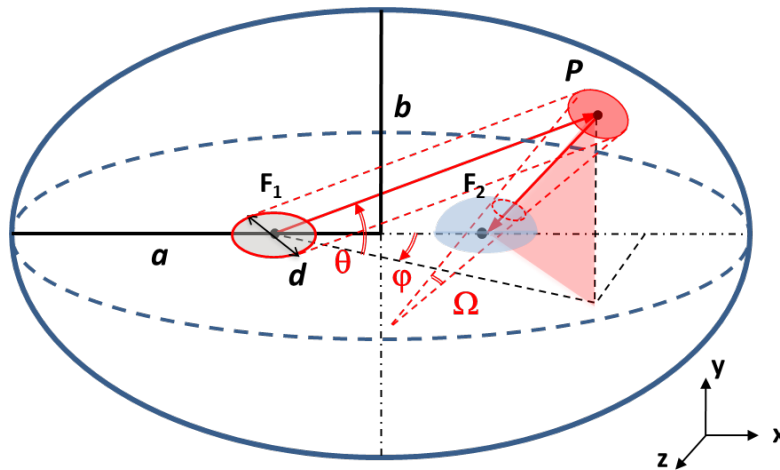


Fig. 1. Principle of a reflective imaging goniophotometer (RIG) with key design parameters for calculation of the angular resolution with a finite size sample of diameter  $d$ : reflective ellipsoid with semi-axis  $a$  and  $b$ , path for optical ray propagating from  $F_1$  to  $F_2$  after reflection at  $P$  (solid red lines), paths for collimated ray bundle scattered from sample converging towards  $F_2$  after reflection on the ellipsoidal dome (dashed red lines).

Note that similar performance should be obtained with a hemispherical dome provided the dimension of the sphere is large relative to the off-center distance of the sample and fisheye camera [9].

#### 3.2. Inherent design limitations

Generally, the higher the sophistication of a goniophotometer, the more difficult is the assessment of performance and the more probable is the occurrence of limitations. If the sample and fisheye lens were infinitely small, ideal BSDF measurements could be performed with the RIG described above. The impact of real finite size components on the performance of the instrument should be properly assessed. We investigate the impact of finite size components on the key parameter in goniophotometry, namely the angular resolution, as well as and on the angular-to-spatial mapping function of the RIG.

##### i) Angular resolution

Angular resolution is obviously a key parameter in goniophotometry. It depends on the specific design of the instrument, as well as on the sample size and measurement angle. For a given direction, a sample of finite size will scatter a bundle of parallel rays that will converge after reflection on the ellipsoidal dome as illustrated in figure 1. The convergence angle, defined by the solid angle  $\Omega$ , sets a fundamental design limit to the angular resolution of the system. The angle  $\Omega$ , which is rotationally non-symmetrical (around the axis defined by P-F<sub>2</sub>), depends on: the sample size ( $d$ ), the dome shape determined by the ellipse axes ( $a$ ,  $b$ ), as well as on the elevation and azimuth angles ( $\theta$  and  $\varphi$ ). To get quantitative figures for the loss of angular resolution inherent to the RIG principle as a function of the various parameters involved, we will consider either the largest or the mean focusing angle (see 3.3).

Note that additional loss of angular resolution can be caused by the performance of the fisheye camera as well as by inaccuracies in the manufacturing of the ellipsoidal dome surface. The contribution from the fisheye lens is generally negligible since a resolution below 1° is common. On the other hand, discrepancies with an ideal ellipsoidal dome shape can have a significant impact on the angular resolution. This point is beyond the scope of this paper.

## ii) Angular-to-space mapping

Let us now take a detailed look into the angular-to-space mapping operation as performed by the fisheye lens in the RIG. The unique feature of fisheye lenses, namely an excellent angular resolution over a large viewing angle, is obtained thanks to significant trade-offs in the optical design, which have far reaching consequences on the RIG angular-to-spatial mapping function.

First, unlike more common lens systems, a fisheye lens uses only a small fraction of its surface for collecting light in a given direction. Indeed, the specific design of a fisheye lens combined with a small aperture stop drastically limits the extent of a collimated beam from a given direction that can reach the sensor plane. This is shown in figure 2 for a typical real fisheye lens modeled in ZEMAX (see 3.3). Only a small bundle of rays (transverse size  $p$ ) out of the large collimated beam of width  $W$  (directly related to the sample size) can penetrate into the camera system without being blocked by the lens aperture stop (not shown). Thus, the actual size of the measured sample portion roughly corresponds to the dimension  $p$  of the ray bundle, whose size is in the order of a few millimeters, i.e. typically a few orders of magnitudes smaller than the size of the fisheye lens. Without such spatial filtering (beam truncation), the sample size would be ultimately limited by the size of the fisheye lens.

Second, the location of the small measured sample portion depends on the measurement angle due to the fisheye lens properties. An ideal angular-to-spatial mapping in the case of a RIG would require the rays from any direction to originate from the same sample portion centered on F<sub>1</sub>. Shall it be the case a ray bundle from any direction would always point exactly towards F<sub>2</sub>. However, this cannot be the case because the spatial filtering inherent to a fisheye lens imposes an off-centered optical path relative to the beam propagation axis pointing towards F<sub>2</sub> (except for the path coincident with the optical axis). The difference between the ideal and real optical paths taken by light from a given direction is illustrated in figure 2 for an incident light beam at 60° relative to the horizontal plane. The ray bundle collected from this direction takes an optical path shifted by a distance  $X$  and points towards a point F<sub>2</sub>'. This means that, by virtue of the ellipse properties, the light flux detected at a given direction of incidence does not originate from an area centered on the ellipse focal point F<sub>1</sub>. Instead, the detected light originates from an area centered on the sample point conjugated to F<sub>2</sub>'.

To assess the impact of the spatial filtering inherent to the angular-to-space mapping function on the RIG principle we need to get quantitative figures for the actual location and size of the areas of the sample measured at each direction.

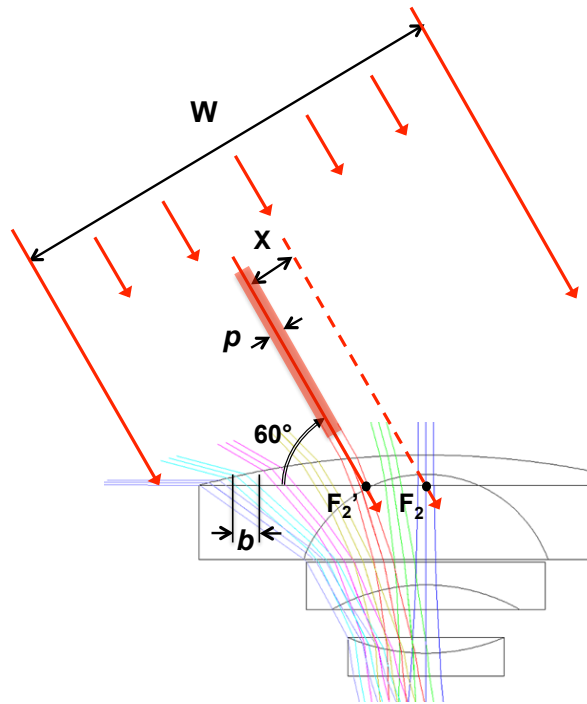


Fig. 2. Artefacts in the angular-to-spatial mapping function in a RIG caused by the fisheye lens properties. Typical fisheye lens modeled in ZEMAX showing the path and extent of ray bundles collected in specific directions for elevation angles ranging from slightly above  $0^\circ$  to  $90^\circ$  with angular steps of  $15^\circ$ . The transverse dimension  $p$  shows the ray bundle size truncated from a light beam of transverse dimension  $W$  at  $60^\circ$  incidence angle. The distance  $X$  shows the offset of the truncated ray bundle path relative to the beam center pointing towards  $F_2'$ . The dimension  $b$  is defined for calculation purposes (see 3.3).

### 3.3. Calculation method and assumptions

A parametric study is ideally suited to investigate the angular resolution and the angular-to-spatial mapping function. It shows how the performance varies as a function of  $\theta$  and  $\varphi$  and allows exploring the dependence on key design parameters.

The propagation of optical rays in the RIG obeys the rules of geometrical optics. Although a mathematical description is relatively straightforward the number of possible trajectories and parameters complicates our investigation. Such a kind of investigation lends itself well to a ray-tracing modeling. Since optical ray-tracing based software tools such as ZEMAX or TracePro do not offer the flexibility required for our parametric study, we developed our own ray-tracing algorithms in Matlab code. The impact on resolution and on the angular-to-space mapping is investigated separately with different codes describing different initial conditions.

For the investigation of the angular resolution we assume a perfect angular-to-spatial mapping function (real fisheye properties not accounted for) and a perfect ellipsoidal dome. For each direction, a beam is defined by a bunch of parallel rays launched from the periphery of the sample of diameter  $d$  centered at  $F_1$ . After reflection on the ellipsoidal dome, a tilt angle relative to the beam axis  $P-F_2$  is calculated for each of these parallel rays. For each pair of opposite peripheral rays, which are equally distributed along the beam periphery, a peripheral focusing angle is calculated by summing the tilt angles obtained. Our results were obtained with 24 peripheral rays (one ray every  $15^\circ$ ), at elevation

and azimuthal angles sampling the hemispherical space in steps of  $15^\circ$  (288 directions). For each direction, we calculate the following two relevant quantitative figures for the angular resolution: the largest and the mean of the peripheral focusing angles.

For the investigation of the angular-to-spatial mapping function we account for typical fisheye properties and again assume a perfect dome. A fisheye lens with very similar properties than the one used in the RIG device [10] was taken from models available in ZEMAX in order to extrapolate the size of the ray bundle collected as well as the coordinates at which it is intercepted by the lens interface ( $F_2'$  in Fig. 2). The size of the ray bundle at the plane x-z, defined by the diameter  $b$ , was found to be nearly constant (2 mm) independent of the direction. To assess the impact on the RIG principle we need to get quantitative figures for the actual location and size of the areas measured on the sample side as a function of the direction of detection. For each coordinate  $F_2'$  related to a detection angle, a bundle of detected parallel rays is defined at the periphery of a disc of diameter  $b$  centered at  $F_2'$ . The rays are launched backwards, i.e. from the fisheye side. The intersections points with the x-z plane can be linked to form a boundary defining the corresponding measured area on the sample side.

## 4. Calculation results

### 4.1. Angular resolution

For a given configuration, i.e. for a given RIG and sample size, quantitative figures for the resolution as a function of the direction of scattering ( $\theta$  and  $\phi$ ) resulting from our calculations (see 3.3) can be represented with a three-dimensional plot.

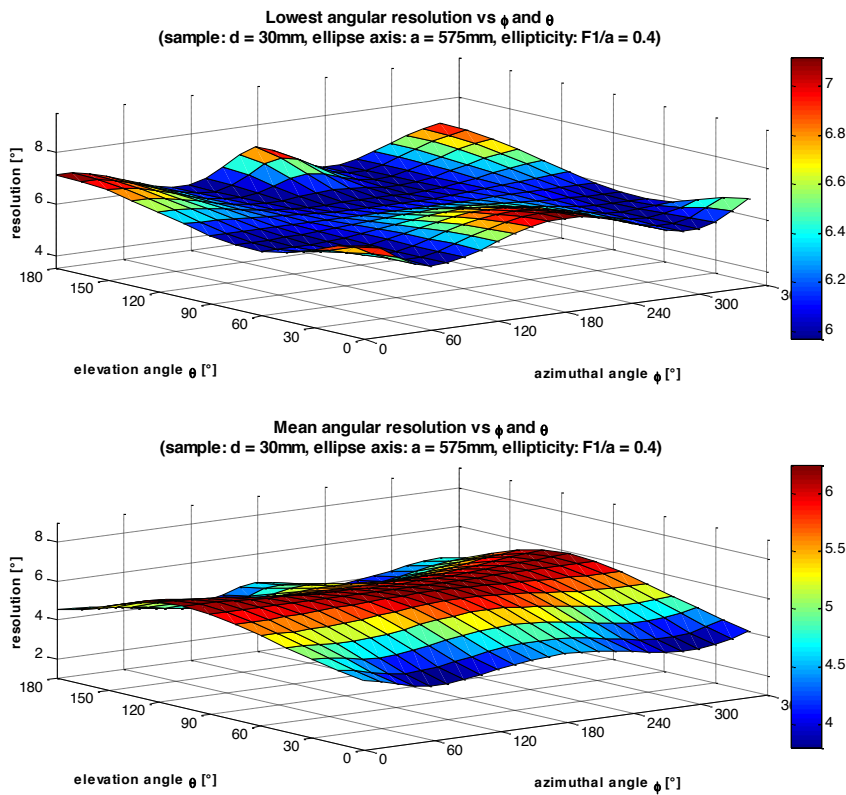


Fig. 3. Calculation results for the lowest and mean angular resolution as function of the elevation and azimuthal angles for a given RIG with  $a = 575\text{mm}$  and  $e = 0.4$ , and a sample  $d = 30\text{mm}$ .

The two plots in figure 3 show the lowest angular resolution and the mean angular resolution (defined in 3.2) as a function of  $\theta$  and  $\varphi$  in steps of  $15^\circ$  (288 directions) for a RIG defined by its semi-axis  $a = 575$  mm and ellipticity  $e = a/F_1 = 0.4$ , and a sample size  $d = 30$  mm.

The calculation results reveal how the resolution depends on direction of measurement. The lowest resolution, corresponding to the highest focusing angle in given direction, lies somewhere above  $6^\circ$  and the average resolution in direction varies around  $5^\circ$ .

It would be interesting to determine, for instance the influence of the sample size on the resolution. For such parametric study, it is preferable to compare average ( $\mu$ ) and standard deviation ( $\sigma$ ) quantities for the values of the three-dimensional plots. These quantities can be advantageously visualized in a two-dimensional bar plot, in which the upper and lower values of each bar correspond to  $\mu + \sigma$  and  $\mu - \sigma$ , respectively. The exact numerical values for  $\mu$  and  $\sigma$  are provided in a table, as well other relevant figures of interest, the average and standard deviation values of the highest angular resolution distribution and the boundary values (lowest and highest resolution). Each pair of average and standard deviation values are extrapolated from a different three-dimensional plot calculated with our Matlab code.

Our parametric study will be performed around a benchmark case, the RIG prototype realized in [10], named “Heliodome”, in which  $a = 575$  mm,  $b = 561$  mm and  $F_1F_2 = 250$  mm. This yields to a factor of ellipticity  $e = a/F_1 = 0.217$ . The sample size taken for benchmark is  $d = 30$ mm, which yields a size ratio, defined as  $d/a$ , of 5% for the Heliodome.

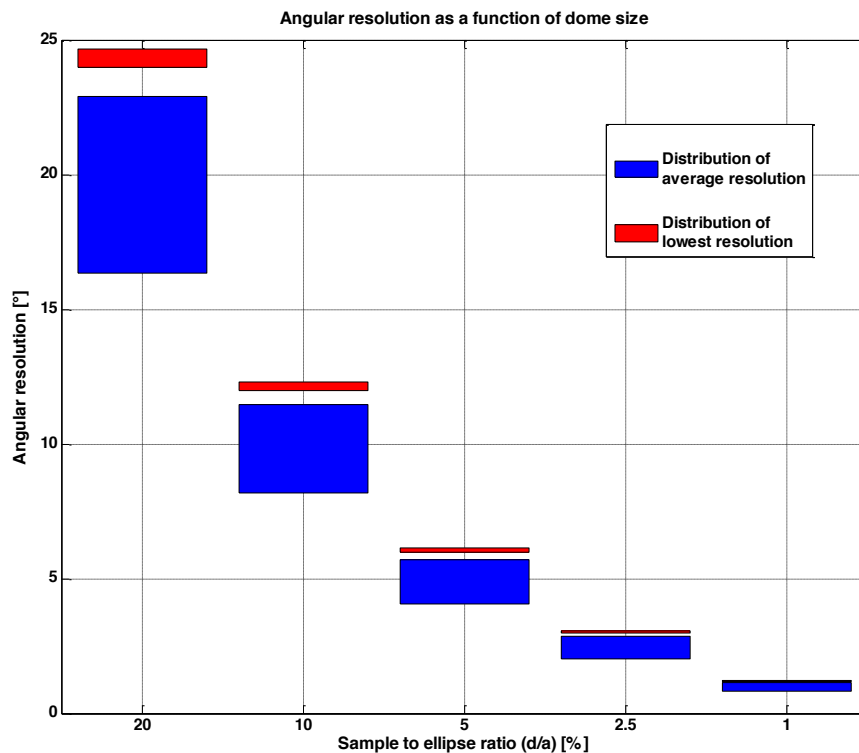


Fig. 4. Calculation results for our parametric study of the angular resolution as a function of the sample size relative to the RIG size. The RIG has a constant size  $a = 575$  mm and ellipticity  $e = 0.217$ . The bars represent the distributions of the average (blue) and lowest (red) angular resolution. Their upper and lower values correspond to  $\mu + \sigma$  and  $\mu - \sigma$ , respectively. The central bar ( $d/a = 5\%$ ) corresponds to the Heliodome case study.

To investigate the dependence on the resolution with the sample size we vary  $d$  in our simulations while maintaining a constant semi-axis length  $a = 575$  mm and a constant factor of ellipticity  $e = 0.217$  mm (Heliodome benchmark case). The results for the relevant figures on resolution are shown in the figure 4 above and table 1 below as a function of the ratio of sample size to the RIG size ( $r = d/a$ ).

Our results provide a quantitative insight into the dependence of the angular resolution with the sample size. In the first approximation, the angular resolution increases linearly with the inverse of the dome size. For a 120 mm large sample, corresponding to a  $d/a$  ratio of 20%, the average angular resolution is around  $20^\circ$  and can be as low as  $24^\circ$ . Such a poor resolution is insufficient by far, for instance, for characterizing a CFS. Accurate measurements, i.e. with an angular resolution higher than  $2.5^\circ$ , can be achieved with a sample smaller than 15mm. Therefore, the measurement of large samples with a sufficient angular resolution, is not possible with the Heliodome design. Improving the performance by increasing the size of the device is likely not a viable option for manufacturing reasons (dome accuracy) as well as for practical and economical reasons (size and cost). For instance, a sample size of 60 mm ( $r = 10\%$ ), a resolution better than  $1^\circ$  would require a roughly ten times larger dome, which is not manageable.

Resolution		Sample to dome size ratio: $r = d/a$ [%]				
		20	10	5	2.5	1
Lowest	$\mu$	24.3	12.1	6.1	3.0	1.2
	$\sigma$	0.36	0.18	0.09	0.04	0.02
Average	$\mu$	19.6	9.8	4.9	2.4	0.98
	$\sigma$	3.29	1.64	0.82	0.41	0.16
Highest	$\mu$	13.0	6.5	3.2	1.6	0.6
	$\sigma$	9.0	4.5	2.3	1.13	0.45
Boundaries	min	25.1	12.6	6.3	3.1	1.3
	max	0.42	0.21	0.10	0.05	0.02

Table 1. Figures for the resolution of the RIG as a function of the sample size. The ratio  $r = 5\%$  corresponds to the Heliodome case study.

#### 4.2. Angular-to-spatial mapping function

The method and the assumptions used for the investigation of the angular-to-spatial mapping function are explained in 3.3. The results of our calculation for the sizes and positions of the sample areas measured by the RIG in a given direction of measurement at  $F_2$  (given by  $\theta$  and  $\varphi$ ) are shown in figure 5. The azimuthal angle  $\varphi$  is varied in steps of  $30^\circ$  from  $0^\circ$  to  $360^\circ$  for the three elevation angles  $\theta$  equal to  $5^\circ$ ,  $30^\circ$  and  $60^\circ$ . The square represents the footprint of a sample of dimension  $d = 20$  mm centered on  $F_1$  to better appreciate the relative sizes of the measured areas.

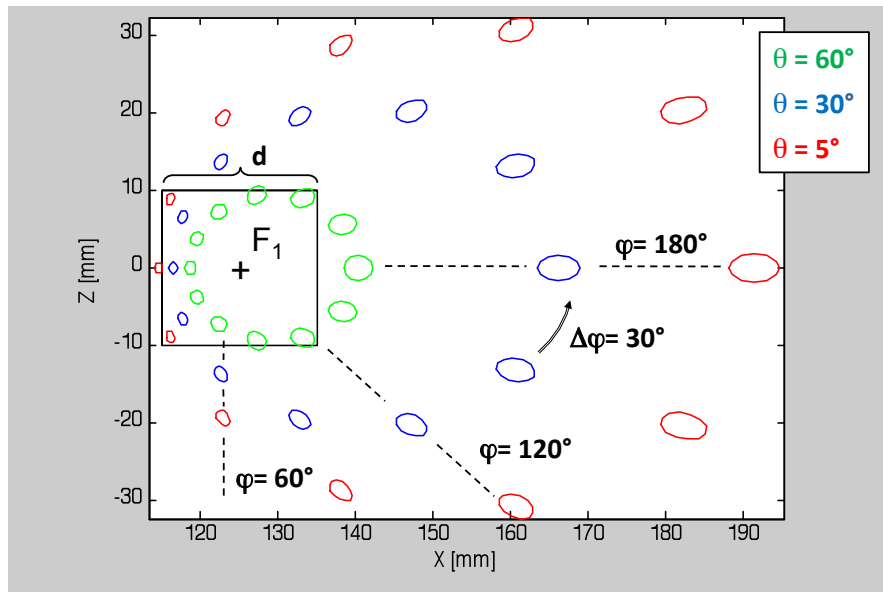


Fig. 5. Calculation results for the size and position of the sample areas measured by the RIG as a function of various directions of measurement at  $F_2$  (given by  $\theta$  and  $\varphi$ ), with a square sample footprint of dimension  $d = 20$  mm centered on  $F_1$  for visual reference.

As expected the measured areas of the sample are very small relative to large samples such as CFSs. The lower the elevation angle, the further away from the center of the sample the areas of measurement are. These limitations and artefacts in the angular-to-spatial mapping function have far reaching consequences as discussed in our conclusion.

## 5. Conclusion

Our results provide a quantitative insight into the dependence of the angular resolution with the sample size for a RIG. For the design parameters used in the Heliodome (existing RIG prototype), we found insufficient angular resolution for characterizing samples larger than a few tens of millimeters like CFSs. A good angular resolution ( $< 2^\circ$ ) is attainable either with samples of relatively small sizes ( $< 10$  mm) or with a RIG of very large dimensions ( $> 5$  m), which is not a viable option.

Moreover, the angular to-space-mapping function of the RIG suffers from severe limitations and artefacts caused by the spatial filtering inherent to the fisheye. Our investigation revealed that, for a given direction of measurement, the area measured on the sample side is relatively small and that its position depends on the direction of detection on the fisheye side. Generally, this can severely bias BSDF measurements with the RIG principle. In the case of a small sample, specific scattering directions would be missing since not collected by the fisheye camera. In the case of a large enough sample to prevent missing angles, a BSDF measurement would contain an angular distribution built with different portions of the same sample. Therefore, based on our investigation, the RIG does not seem to be a viable solution for measuring BSDF of large objects such as CFSs.

## References

- [1] K.M. Beauchemin, P. Hays, Journal of the Royal Society of Medicine, 91 (1998), 353-354.
- [2] A. Laouadi, A. Parekh, Lighting Research and Technology, 39 (2007), 109-122.

- [3] L.G. Ward, R. Shakespeare, (1997). *Rendering with Radiance: The Art and Science of Lighting Visualization*. San Francisco: Morgan Kaufmann Publishers.
- [4] Commission Internationale de l'Eclairage. Radiometric characteristics of material and their measurements. CIE 38 (TC-2.3), 1977.
- [5] M. Lindemann, R. Maass, G. Sauter, *Light and Engineering*, 20 (2012), 97-112.
- [6] M. Andersen, J. de Boer, *Energy and Buildings*, 38 (2006), 836 – 848.
- [7] P. Boher, M. Luet, T. Leroux, *Optical Metrology in Production Engineering*, SPIE 5457, (2004), 344-354.
- [8] S. Wadman, S. Baumer, *Surface Scattering and Diffraction III*, SPIE 5189, (2003), 163-173.
- [9] G. Ward, *Computer Graphics* 26 (2006), 265-272.
- [10] M. Andersen, E. Stokes, N. Gayeski, C. Browne, *Solar Energy*, 84 (2009), 549-562.